Supporting Information

A Pyrene-based, Fluorescent Three-dimensional Covalent Organic Framework

Guiqing Lin,[†] Huimin Ding,[†] Daqiang Yuan,[‡] Baoshan Wang[*,†] and Cheng Wang[*,†]

[†] Key Laboratory of Biomedical Polymers (Ministry of Education), College of Chemistry and Molecular Sciences, Wuhan University, Wuhan 430072, China

Email: chengwang@whu.edu.cn

[‡] State Key Laboratory of Structural Chemistry, Fujian Institute of Research on the Structure of Matter, Chinese Academy of Sciences, Fuzhou 350002, China

Section S1. Materials and Methods

Acetone, ethanol, tetrahydrofuran, *o*-dichlorobenzene, *n*-butanol, dichloromethane, chloroform, *N,N*-dimethyl formamide and aniline were purchased from Acros. Dehydrated solvents were obtained after treating solvents with standard procedures. TFPPy[S1] and TAPM[S2] were synthesized according to the literature.

^{1}H NMR spectra were measured on a Bruker Fourier 300 M spectrometer. Solid-state NMR spectra were recorded at ambient temperature on a Bruker AVANCE III 400M spectrometer. High resolution MALDI–TOF data was collected on Bruker Solarix. Elemental analysis was conducted on a Flash EA 1112. Fourier transform infrared (FT-IR) spectra were recorded on a NICOLET 5700 FTIR Spectrometer. Powder X-ray diffraction (PXRD) patterns were obtained on a Rigaku Smartlab X-Ray diffractometer with Cu Kα line focused radiation at 40 kV and 40 mA from 2θ = 2.0° up to 40° with 0.02° increment. Thermogravimetric analysis (TGA) from 20-800 °C was carried out on a PerkinElmer TG-DTA6300 in nitrogen atmosphere using a 10 °C/min ramp without equilibration delay. Field-emission scanning (FE-SEM) was performed on a Zeiss ΣIGMA operating at an accelerating voltage ranging from 0.1 to 30 kV. The sample was prepared by dispersing the material onto conductive adhesive tapes attached to a flat aluminum sample holder and then coated with gold. Fluorescence spectra were recorded on a HITACHI F-4600 spectrofluorometer. Molecular modeling was carried out using *Materials Studio* suite of programs (Accelrys Inc.).

The nitrogen isotherms were measured at 77 K using an Autosorb-iQ

(Quantachrome) surface area size analyzer. Before measurement, the samples were degassed in vacuum at 100 °C for 12 h. N_2 and CO_2 physisorption isotherms were measured up to 1 bar at 273 K and 295 K using a Micrometrics ASAP 2020-M surface area analyzer. Prior to measurements, samples were degassed for over 12 h at 100 °C. UHP grade N_2 and CO_2 were used for measurements. Oil-free vacuum pumps and oil-free pressure regulators were used for measurements to prevent contamination of the samples during the degassing process and isotherm measurement.

Section S2. Chemical Synthesis

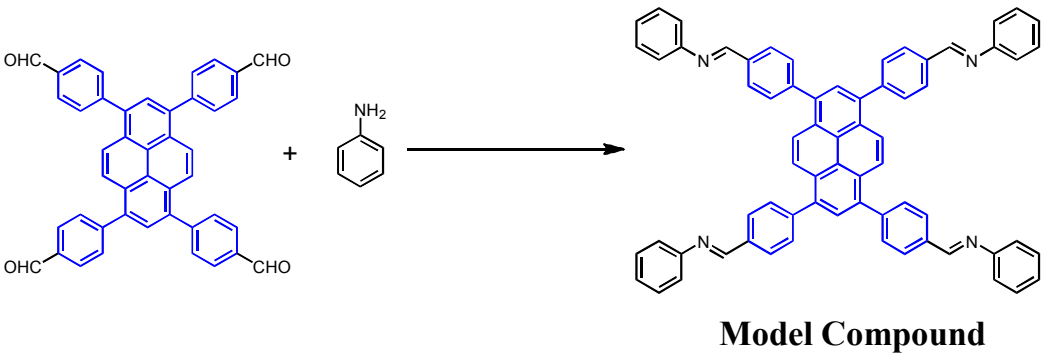

Model Compound

Scheme S1 Synthesis of model compound

Synthesis of model compound: TFPPy (100 mg, 0.161 mmol) and aniline (0.1 mL, 1.10 mmol) were added to ethanol (15 mL) and chloroform (15 mL), and the mixture was refluxed for one night. The precipitate was filtered and washed with ethanol and acetone and dried to get yellow green solid (124 mg, 84% yield). ^{1}H NMR (300 MHz, CD_2Cl_2, ppm): δ = 8.64 (s, 4H), 8.29 (s, 4H), 8.20-8.08 (m, 10H), 7.86 (d, *J* = 7.3 Hz, 8H), 7.45 (t, *J* = 7.7 Hz, 8H), 7.35-7.22 (m, 12H). HR-MS (MALDI–TOF): calcd for $C_{68}H_{46}N_4$ m/z = 919.37560 $[M+H]^+$, found: m/z =919.37903 $[M+H]^+$.

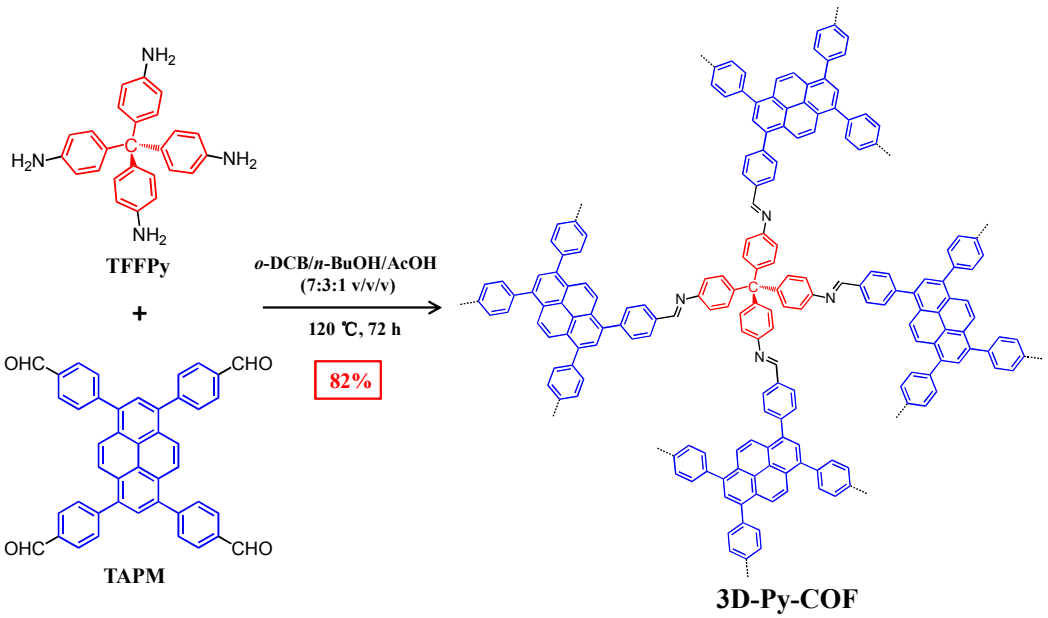

Scheme S2 Synthesis of 3D-Py-COF

Synthesis of 3D-Py-COF. A Pyrex tube was charged with TAPM (5.7 mg; 0.015 mmol), TFFPy (9.3 mg; 0.015 mmol), 0.7 mL *o*-dichlorobenzene, 0.3 mL *n*-butanol and 0.1 mL of 6 M aqueous acetic acid. After being degassed by freeze-pump-thaw technique for three times and then sealed under vacuum, the tube was placed in an oven at 120 °C for 72 h. The resulting precipitate was filtered, washed with anhydrous tetrahydrofuran and extracted by Soxhlet extractor for 24 h. The solid was dried at 80 °C under vacuum for 12 h to afford yellow powder (12.3 mg, 82% yield). Elemental analysis for the calculated: C, 89.39%; H, 4.57%; N, 6.04%. Found: C, 84.59%; H, 4.65%; N, 5.61%.

Section S3. Characterization of 3D-Py-COF

A. FT-IR Spectroscopy Analysis

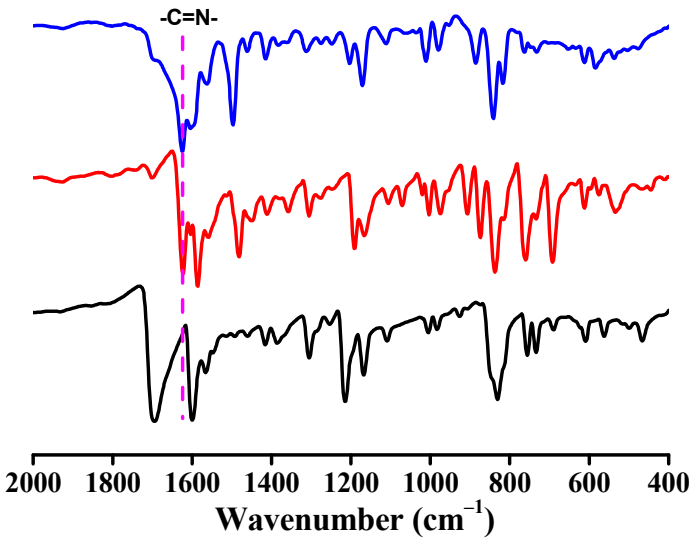

Figure S1 FT-IR spectra of TFPPy (black curve), model compound (red curve) and 3D-Py-COF (blue curve). The appearance of a new band at 1626 cm^{-1} in 3D-Py-COF confirmed the formation of imine linked C=N.

B. ^{13}C Solid-State NMR Spectroscopy

High resolution solid-state NMR spectra were recorded at ambient pressure on a Bruker AVANCE III 400M spectrometer using a standard CP-TOSS pulse sequence (cross polarization with total suppression of sidebands) probe with 4 mm (outside diameter) zirconia rotors. Cross-polarization with TOSS was used to acquire ^{13}C data at 100.37 MHz. The ^{13}C ninety-degree pulse widths were 4 μs. The decoupling frequency corresponded to 72 kHz. The TOSS sample-spinning rate was 5 kHz. Recycle delays was 2s. The ^{13}C chemical shifts are given relative to glycine as 176.03 ppm. ^{13}C NMR: δ = 156.24, 148.57, 144.27, 135.92, 128.19, 125.60, 114.93, 63.56.

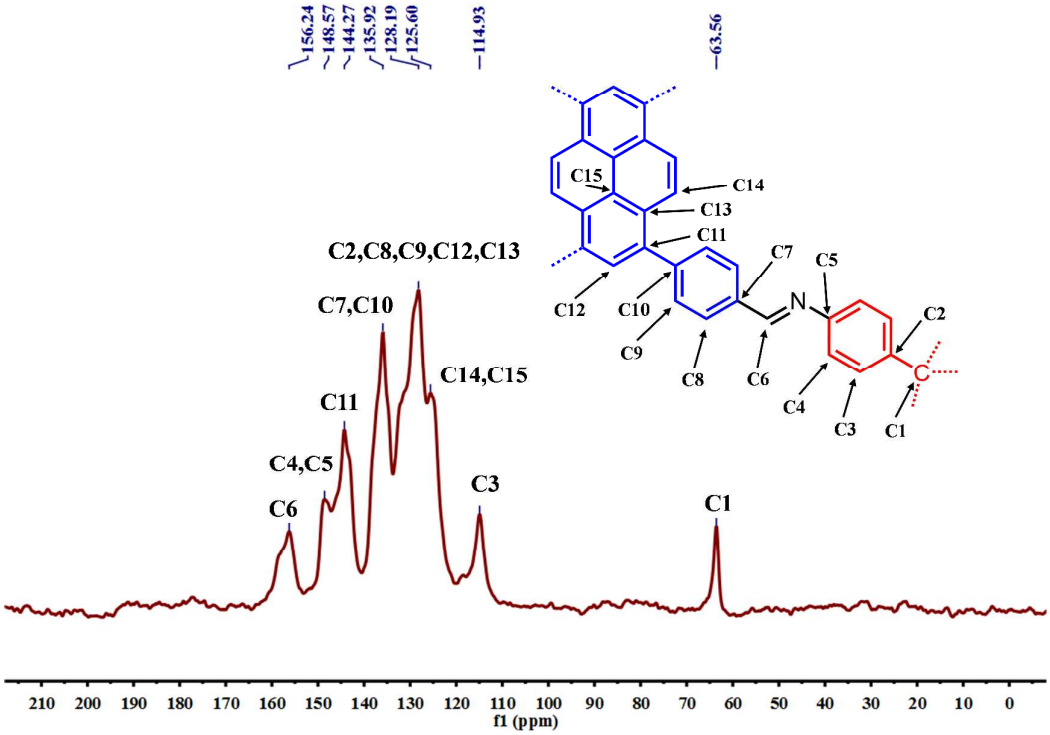

Figure S2 ^{13}C Solid-State NMR spectrum of 3D-Py-COF.

C. Thermogravimetric Analysis of 3D-Py-COF

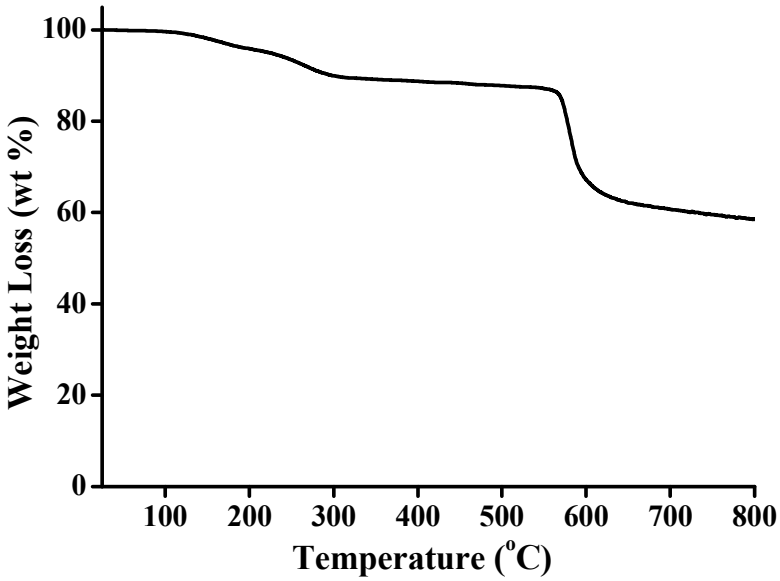

Figure S3 TGA profile of 3D-Py-COF

D. Nitrogen Sorption Isotherm measurements for 3D-Py-COF

Before measurement, the samples were degassed in vacuum at 100 °C for 12 h. A liquid N_2 bath was used for adsorption measurements at 77 K. To provide high accuracy and precision in determining P/P_0, the saturation pressure P_0 was measured throughout the N_2 analyses by means of a dedicated saturation pressure transducer, which allowed us to monitor the vapor pressure for each data point. The Brunauer-Emmett-Teller (BET) method was utilized to calculate the specific surface areas. To estimate pore size distributions for 3D-Py-COF, N_2 isotherms were analyzed using quenched solid density functional theory (QSDFT) for N_2 adsorption at 77 K based on a carbon model containing slit/cylindrical pores. By using QSDFT adsorption branch model, the pore volume (0.72 cm^3 g^{-1}) was derived from the adsorption curve, which is lower to calculated value (1.73 cm^3 g^{-1})[S3]. This difference could be explained by the tapping of some impurities (e.g. starting material) in the narrow pore (0.59 nm), which may block the access of the pore.

E. Scanning Electron Microscopy Imaging of 3D-Py-COF

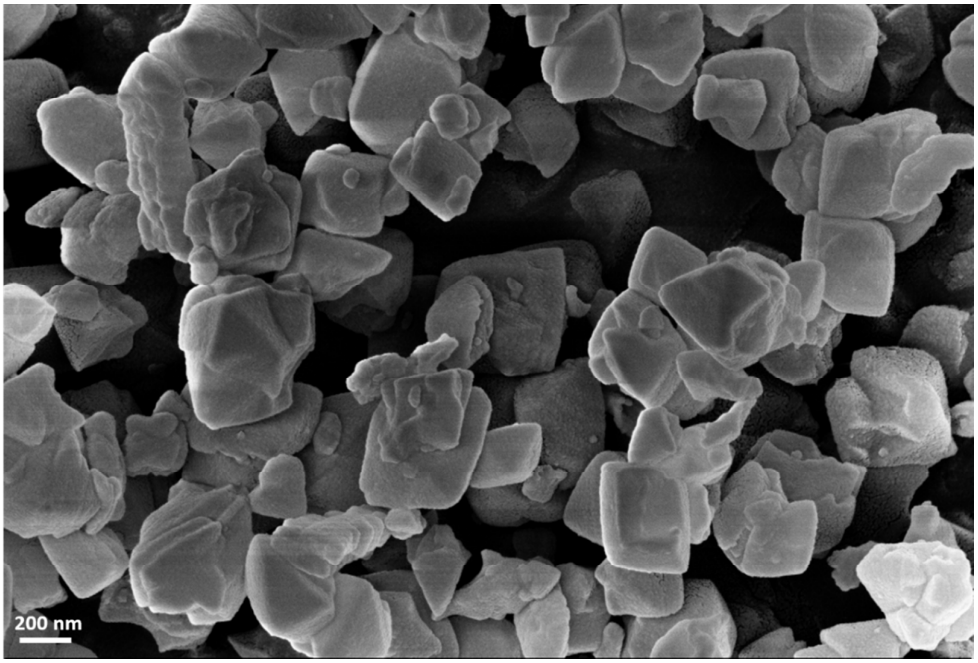

Figure S4 SEM image of 3D-Py-COF

Section S4. Structure Simulation

The 3D-Py-COF models were generated using Materials Studio suite of programs. Vertex positions were obtained from Reticular Chemistry Structure Resource (RCSR). The unit cell structures of 3D-Py-COF were calculated using the density-functional tight-binding method (DFTB) including Lennard-Jones dispersion, as implemented in the DFTB+ program package. DFTB is an approximate density functional theory method based on the tight binding approach and utilizes an optimized minimal LCAO Slater-type all-valence basis set in combination with a two-center approximation for Hamiltonian matrix elements. The Coulombic interaction between partial atomic charges was determined using the self-consistent charge (SCC) formalism. Lennard-Jones type dispersion was employed in all calculations to describe van der Waals and π-stacking interactions. The lattice dimensions were optimized simultaneously with the geometry. The standard DFTB parameters for X–Y element pairs (X, Y = C, H, N) interactions were selected from the mio-1-1 set.

Pawley refinement was carried out using Reflex, a software package for crystal determination from XRD pattern. Unit cell dimension was set to the theoretical parameters. The Pawley refinement was performed to optimize the lattice parameters iteratively until the wR_P value converges and the overlay of the observed with refined profiles shows good agreement. The pseudo-Voigt profile function was used for whole profile fitting and Berrar–Baldinozzi function was used for asymmetry correction during the refinement processes. Line broadening from crystallite size and lattice strain was considered.

For 3D-Py-COF, considering the geometry of the precursors and the connection patterns, only a few topologies (eg. **pth**, **pti**, **ptt**, **pts**, *etc.*) are reasonable according to RCSR. The lattice models (e.g., cell parameters, atomic positions, and total energies) were then fully optimized using DFTB method. For **pth**, **pti** and **ptt** nets, the major peaks of the calculated PXRD patterns (Figure S5) appeared below 7 degree, which cannot fit to the experimental data.

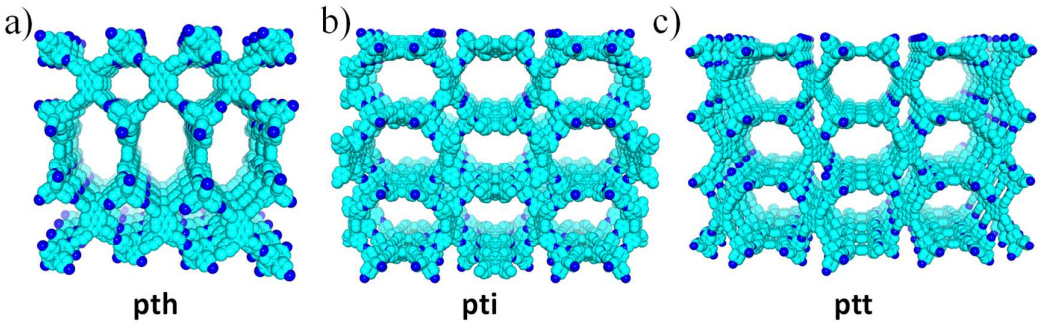

Figure S5 Space-filling models of 3D-Py-COF with different nets: a) **pth**, b) **pti**, c) **ptt**. Carbon, cyan; Nitrogen, blue; Hydrogen atoms are omitted.

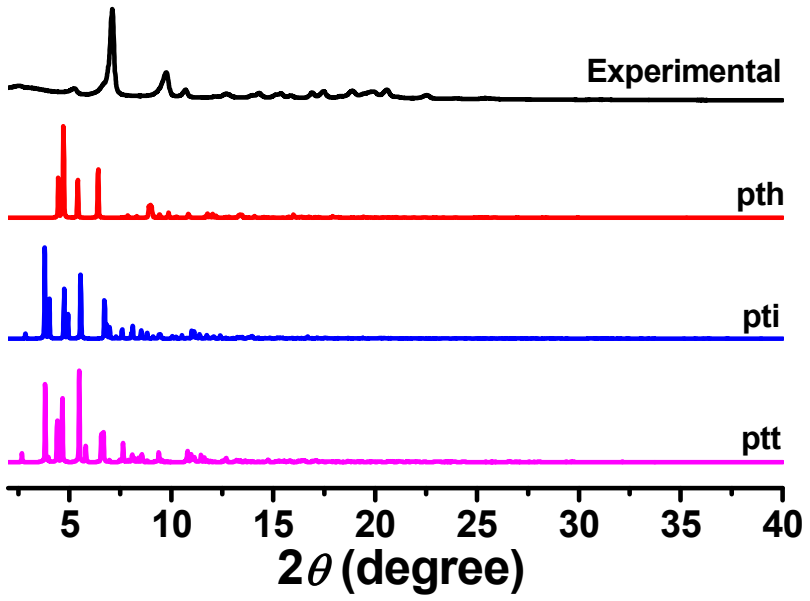

Figure S6 The calculated PXRD profiles: **pth** (red), **pti** (green), **ptt** (magenta). The experimental pattern was also presented (black).

For **pts** net, we have simulated several different structures (Figure S7). For **pts-a** ($P4_2/mmc$ space group) and non-interpenetrated **pts** topologies ($Pmmm$ space group), the major peaks of the calculated PXRD patterns (Figure S8) appeared below 7 degree, which cannot fit to the experimental data. For distorted 2-fold interpenetrated **pts** topology ($Pmc2_1$ space group), although the calculated electronic energy is even lower, the calculated PXRD pattern (Figure S8) has shown several peaks below 5 degrees that disagree with the experimental data. For 2-fold interpenetrated **pts** topology ($Cmmm$ space group, also see Figure 2 in maintext), the calculated PXRD pattern was in agreement with experimental data. In addition, Pawley refinement yielded an XRD pattern that is in good agreement with the experimental data and the wR_P and R_P values was 8.29 and 5.41%.

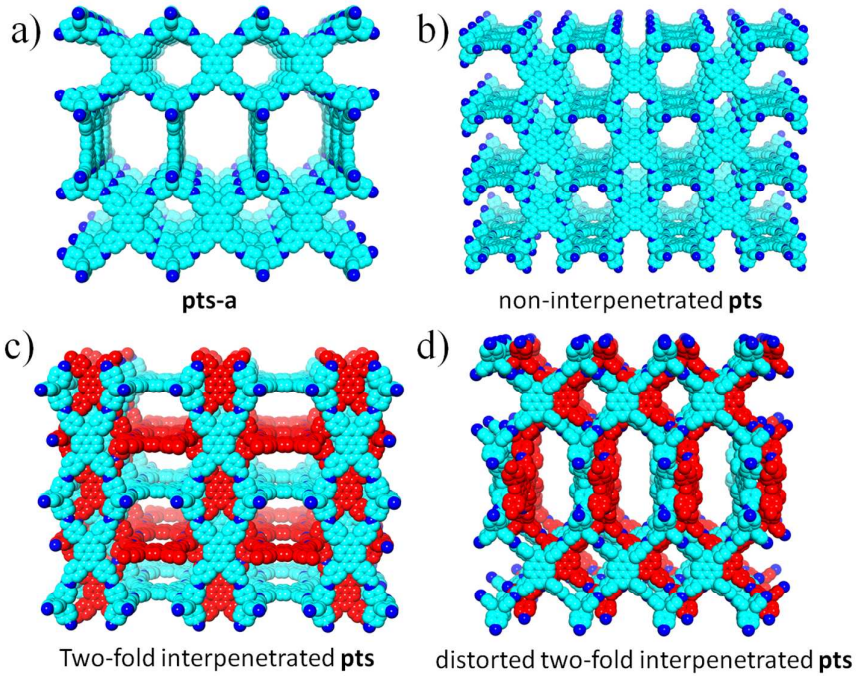

Figure S7 Space-filling models of 3D-Py-COF with **pts** net: a) **pts-a**, b) non-interpenetrated **pts**, c) two-fold interpenetrated **pts**, d) distorted 2-fold interpenetrated **pts**. Carbon, red or cyan; Nitrogen, blue; Hydrogen atoms are omitted.

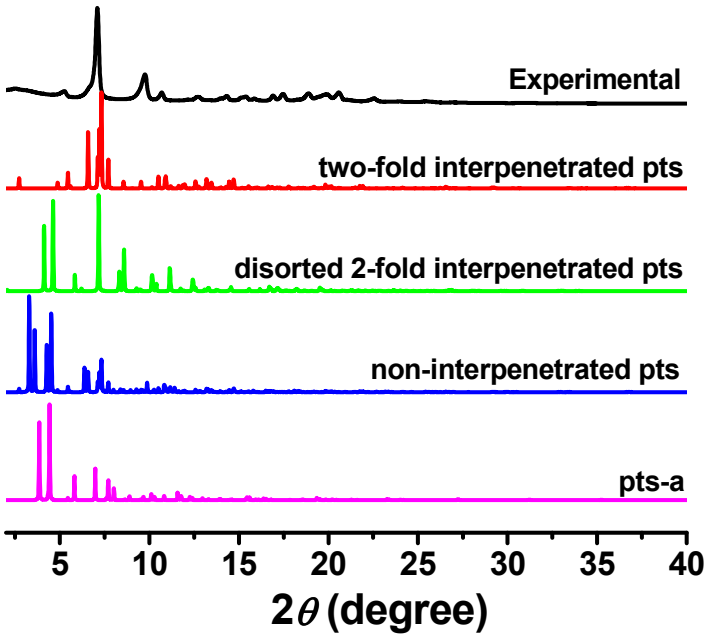

Figure S8 The calculated PXRD profiles: two-fold interpenetrated **pts** (red), distorted two-fold interpenetrated **pts** (green), non-interpenetrated **pts** (blue) and **pts-a** (magenta). The experimental pattern was also presented (black).

Since pyrene is axial symmetry (2D C_2), we had also considered other alternative structure of two-fold interpenetrated **pts** topology. For example, we simulated two-fold interpenetrated **pts** topology with $P4_2/mcm$ space group (Figure S9), in which the pyrene units has the same orientations in the 3D network. However, as shown in Figure S10, the calculated PXRD pattern has shown less peaks compared to the experimental data, especially the peaks at 6.6 (the shoulder of dominant peak) and 9.7 degrees are missing. In addition, the Pawley refinement yielded an XRD pattern that is different with experimental pattern, as evident by their big difference compared to the experimental data. In this model, the wR_p and R_p values converged to 25.36 and 16.71%. Based on these calculations, 3D-Py-COF is proposed to have a two-fold interpenetrated **pts** topology with *Cmmm* space group.

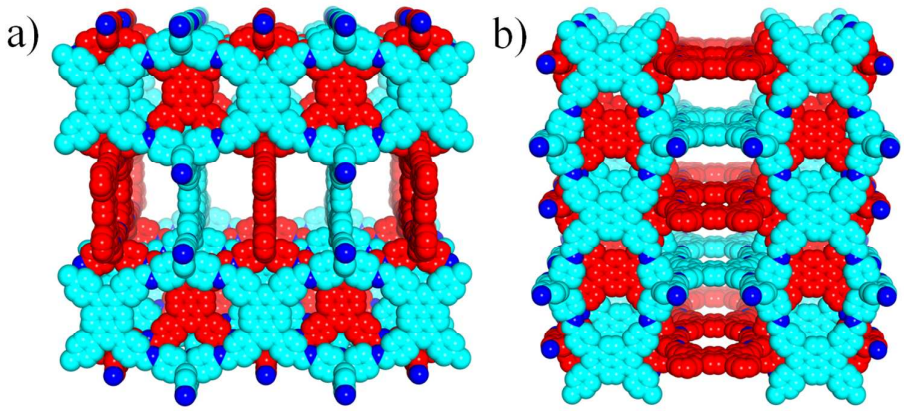

Figure S9 Space-filling models of 3D-Py-COF adopting two-fold interpenetrated **pts** topology with $P4_2/mcm$ space group. Carbon, red or cyan; Nitrogen, blue; Hydrogen atoms are omitted.

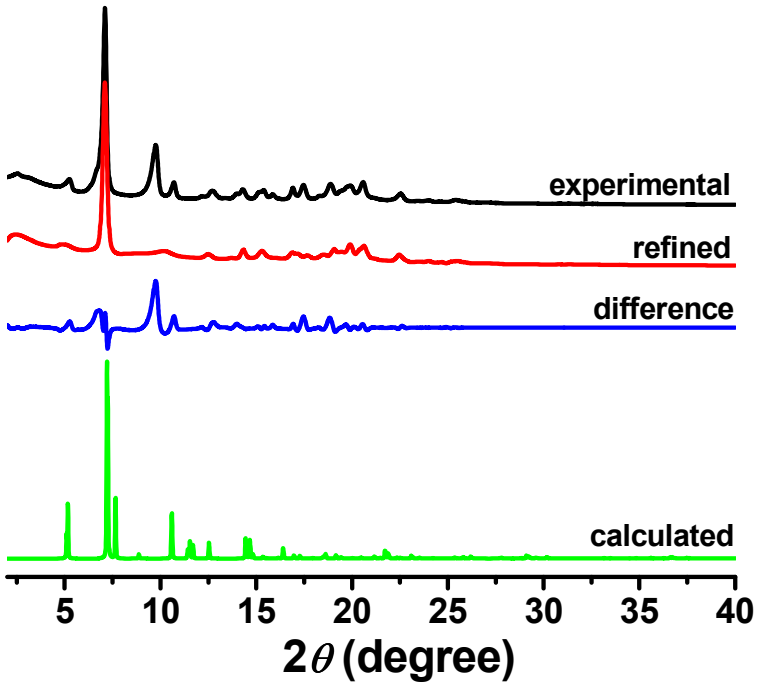

Figure S10 PXRD patterns of 3D-Py-COF adopting two-fold interpenetrated **pts** topology with $P4_2/mcm$ space group: experiment pattern (black curve), Pawley refined (red curve) and calculated (green curve) pattern, the difference between experimental and calculated data (blue curve).

Table S1 Fractional atomic coordinates for the unit cell of two-fold interpenetrated **pts** net with *Cmmm* space group.

two-fold interpenetrated **pts**	Space group: *Cmmm* a = 24.8910 Å, b = 27.1822 Å, c = 32.5284 Å $\alpha = \beta = \gamma = 90.0°$		
H	0.50000	0.77031	0.59142
H	0.50000	0.59815	0.63424
H	0.50000	0.65841	0.68367
H	0.50000	0.75047	0.70592
H	0.50000	0.88564	0.62173
H	0.50000	0.96506	0.64677
H	0.50000	0.91050	0.77194
H	0.50000	0.17348	0.74346
C	0.50000	0.55365	0.46168
C	0.50000	0.60682	0.46066
C	0.50000	0.64435	0.42277
C	0.50000	0.73195	0.39943
C	0.50000	0.71928	0.35813
C	0.50000	0.75892	0.32659
N	0.50000	0.80399	0.33983
C	0.50000	0.85070	0.31968
C	0.50000	0.85772	0.27713
C	0.50000	0.89133	0.34529
C	0.50000	0.90595	0.26114
C	0.50000	0.93888	0.32973
C	0.50000	0.94836	0.28704
C	0.50000	0.30338	0.43014
C	0.50000	0.33053	0.34833
C	0.50000	0.52524	0.57370
H	0.50000	0.71504	0.54087
C	0.50000	0.63314	0.37945
H	0.50000	0.46060	0.60325
H	0.24008	0.00000	0.12539

H	0.05707	0.00000	0.18073
H	0.12937	0.00000	0.22560
H	0.23035	0.00000	0.24082
H	0.37393	0.00000	0.15257
H	0.46162	0.00000	0.17714
H	0.40314	0.00000	0.30259
H	0.68849	0.00000	0.27510
C	0.04965	0.00000	0.95476
C	0.09535	0.00000	0.97895
C	0.10145	0.00000	0.87947
C	0.19926	0.00000	0.86290
C	0.19045	0.00000	0.82079
C	0.23680	0.00000	0.79208
N	0.28486	0.00000	0.80768
C	0.33660	0.00000	0.78847
C	0.34505	0.00000	0.74598
C	0.38064	0.00000	0.81453
C	0.39779	0.00000	0.73046
C	0.43291	0.00000	0.79934
C	0.44368	0.00000	0.75669
C	0.84302	0.00000	0.89093
C	0.86237	0.00000	0.80712
C	0.05118	0.00000	0.09000
H	0.13387	0.00000	0.96794
H	0.17439	0.00000	0.07993
C	0.90535	0.00000	0.83524
C	0.50000	0.00000	0.73489
C	0.00000	0.00000	0.02281
C	0.00000	0.00000	0.89126
H	0.00000	0.00000	0.85989
C	0.50000	0.47299	0.50000
C	0.50000	0.37157	0.50000
H	0.50000	0.33494	0.50000

Section S5. Gas absorption and separation

In order to compare the efficacy of 3D-Py-COF for CO_2/N_2 separation, we used the Ideal Adsorbed Solution Theory (IAST) of Myers and Prausnitz along with pure component isotherm fits to determine the molar loadings in the mixture for specified partial pressures in the bulk gas phase.[S4]

The measured experimental data on pure component isotherms for CO_2 and N_2, in terms of excess loadings, were first converted to absolute loading using the Peng-Robinson equation of state for estimation of the fluid densities. The pore volume of 3D-Py-COF used for this purpose was 0.72 cm^3 g^{-1}. The absolute component loadings at 273 K were fitted with a single-site Langmuir-Freundlich model (Eq. 1), where *a* is saturation capacity and *b* and *c* are constants.

$$N = \frac{abP^c}{1+bP^c} \qquad \text{(Eq. 1)}$$

The adsorption selectivity, S_{ads}, is for binary mixtures defined by Eq. 2, where x_i is the mole fractions of component i in the adsorbed phases and y_i is the mole fractions of component i in the bulk phases.

$$S_{ads} = \frac{x_1/x_2}{y_1/y_2} \qquad \text{(Eq. 2)}$$

The isosteric heat of adsorption Q_{st} was calculated based on gas adsorption isotherms under different temperatures according to virial method.[S5] The isotherms were fitted to Eq. 3.

$$\ln P = \ln N + \frac{1}{T}\sum_{i=0}^{m} a_i N^i + \sum_{i=0}^{n} b_i N^i \qquad \text{(Eq. 3)}$$

In Eq. 3, *P* is the pressure, Pa; *N* is gas uptake, mmol g^{-1}; *T* is the absolute temperature, K; a_i and b_i are virial constants, and *m* and *n* are coefficients used to

describe the isotherms.

The following equation (Eq. 4) was used to calculate the isosteric heat of adsorption, where *R* is the universe gas constant.

$$Q_{st} = -R\sum_{i=o}^{m} a_i N^i \qquad \text{(Eq. 4)}$$

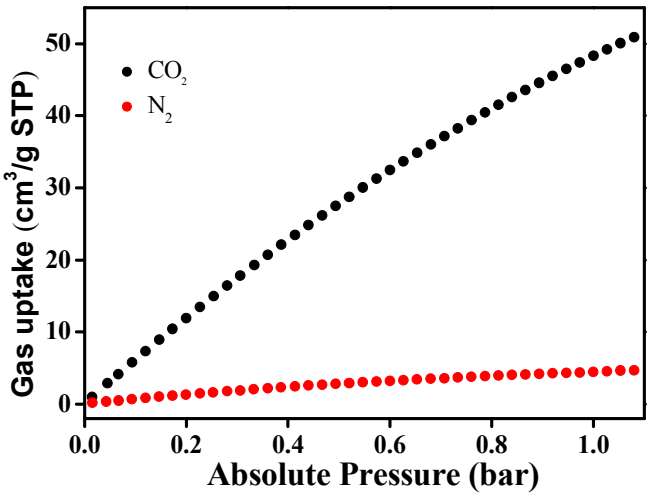

Figure S11 CO_2 and N_2 isotherms at 295 K

The origin of the CO_2/N_2 selectivity may be from the narrow pore size or the strong affinity between CO_2 with imine group. However, the experimental PSD data show that the minima pore size is ~5.9 Å, which is larger than the kinetic diameter of N_2 (3.64 Å) and CO_2 (3.3 Å). So the major contribution to the selectivity is not due to narrow pore or molecular sieve effect. We infer that the strong affinity between CO_2 with imine group results in the origin of the selectivity. The binding energies between CO_2/N_2 and COF have been calculated using the DFTB-D method. It was found that the CO_2 molecule prefers to be absorbed at the imine site by forming a N...CO_2 complex with the binding energy of 12.9 kJ mol^{-1}. In contrast, the absorption energy for N_2 molecule is only 7.5 kJ mol^{-1}, which is about half of that for CO_2. The

selectivity for CO_2/N_2 is estimated to be $e^{-\Delta E/RT} \sim 11$ at 273K, which is in reasonable agreement with the low-pressure limit experimental results.

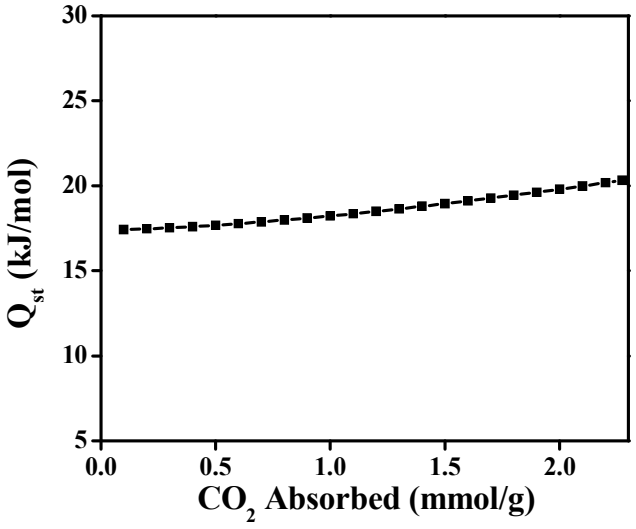

Figure S12 Heat of adsorption plot of CO_2 adsorption for 3D-Py-COF

Section S6. Spectroscopic Properties

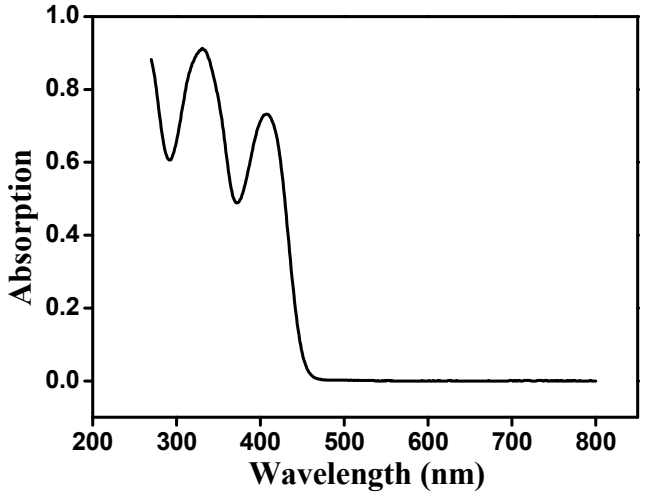

Figure S13 UV spectrum of model compound (2×10^{-5} M in DMF)

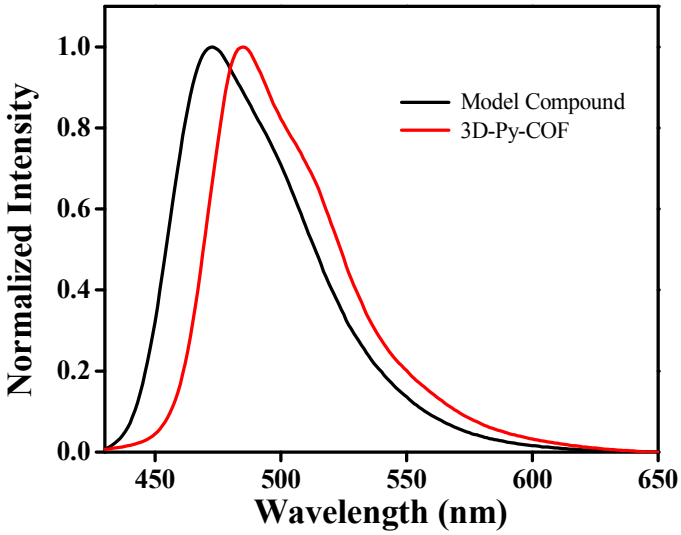

Figure S14 Normalized fluorescence spectra of model compound and 3D-Py-COF in DMF upon excitation at 408 nm.

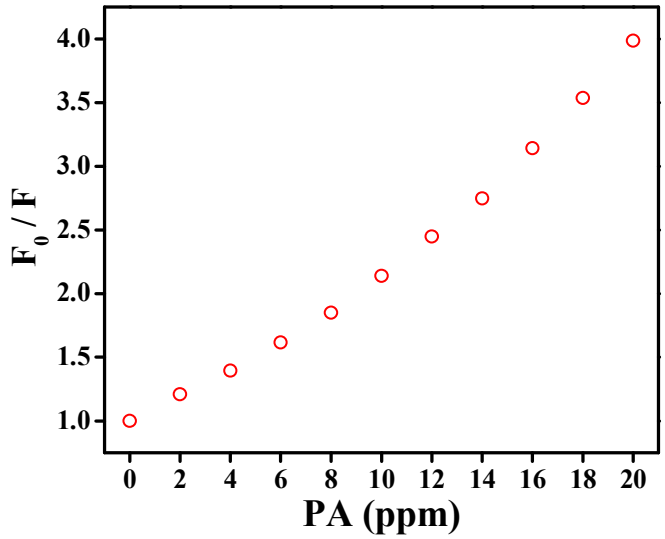

Figure S15 The Stern-Volmer plots obtained from titration of 3D-Py-COF with PA.

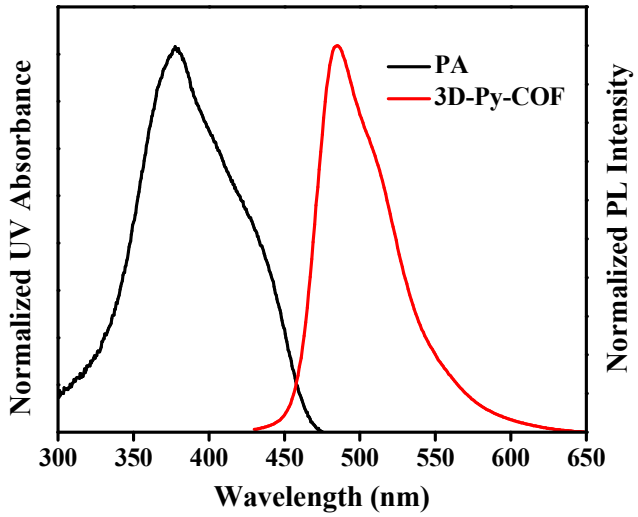

Figure S16 Absorption spectrum of PA and PL spectra of 3D-Py-COF in DMF

The fluorescent quenching of 3D-Py-COF on addition of PA is most likely due to an electron transfer mechanism. By using the DFTB-D method, the HOMOs and LUMOs energy levels of 3D-Py-COF (E_{HOMO} = -5.41 eV, E_{LUMO} = -3.86 eV) and PA (E_{HOMO} = -7.57 eV, E_{LUMO} = -4.88 eV) were evaluated. It is evident that the LUMO of PA is much lower than that of 3D-Py-COF, and is close to the HOMO of 3D-Py-COF, indicating the electron transfer from the HOMO of 3D-Py-COF to the LUMO of PA is facilitated upon photoexcitation. In addition, partially spectral overlap between the 3D-Py-COF emission and PA absorption was found. Thus, resonance energy transfer may occur when the distance between 3D-Py-COF and PA is appropriate (3D-Py-COF could offer cavities for PA to enter in), which may also contribute to fluorescence quenching in some degree.

Section S7. ^{1}H NMR Spectrum

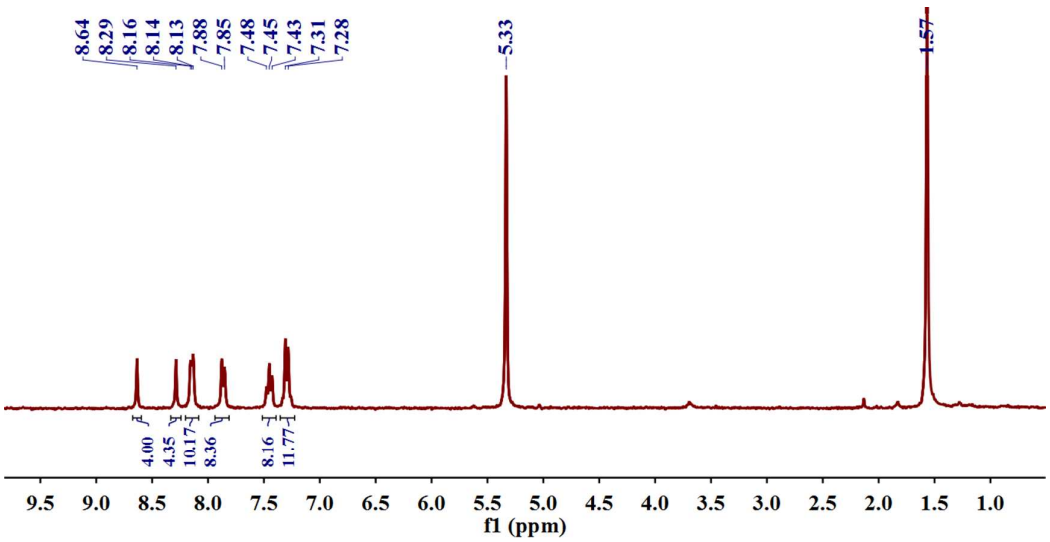

Figure S17 ^{1}H NMR spectrum (CD_2Cl_2, 300 MHz) of model compound.

Section 8. References

S1 Rabbani, M. G.; Sekizkardes, A. K.; Kahveci, Z.; Reich, T. E.; Ding, R.; El-Kaderi, H. M. *Chem. Eur. J.* **2013**, *19*, 3324–3328.

S2 Ganesan, P.; Yang, X.; Loos, J.; Savenije, T. J.; Abellon, R. D.; Zuilhof, H.; Sudhölter, E. J. R. *J. Am. Chem. Soc*. **2005**, *127*, 14530–14531.

S3 Bae, Y.-S.; Yazaydın, A. Ö.; Snurr, R. Q. *Langmuir*, **2010**, *26*, 5475–5483.

S4 Myers, A. L.; Prausnitz, J. M. *AIChE J*. **1965**, *11*, 121–127.

S5 Zhu, Y.; Wan, S.; Jin, Y.; Zhang, W. *J. Am. Chem. Soc*. **2015**, *137*, 13772–13775.

Reference 46 in the maintext

Liu, Y.; Ma, Y.; Zhao, Y.; Sun, X.; Gándara, F.; Furukawa, H.; Liu, Z.; Zhu, H.; Zhu, C.; Suenaga, K.; Oleynikov, P.; Alshammari, A. S.; Zhang, X.; Terasaki, O.; Yaghi, O. M. *Science*, **2016**, *351*, 365–369.